



**Microfluidics-enabled Rational Design for Ag-ZnO
Nanocomposite Films for Enhanced Photoelectrochemical
Performance**

Journal:	<i>CrystEngComm</i>
Manuscript ID	CE-ART-08-2019-001316.R1
Article Type:	Paper
Date Submitted by the Author:	21-Nov-2019
Complete List of Authors:	Jun, Ho Young; Yeungnam University, Chemical Engineering Chang, Chih-hung; Oregon State University, School of Chemical, Biological, and Environmental Engineering Ahn, Kwang-Soon; Yeungnam University, School of Chemical Engineering Ryu, Si Ok; Yeungnam University, School of Chemical Engineering Choi, Chang-Ho; Gyeongsang National University,

Microfluidics-enabled Rational Design for Ag-ZnO Nanocomposite Films for Enhanced Photoelectrochemical Performance

Ho Young Jun,^a Chih-Hung Chang,^b Kwang-Soon Ahn,^a Si Ok Ryu^{*a} and Chang-Ho Choi^{*c}

Received 00th January 20xx,
Accepted 00th January 20xx

DOI: 10.1039/x0xx00000x

Ag-ZnO nanocomposite film has been widely employed as a promising photocatalyst displaying the excellent charge separation and broadband absorption under illumination. Although a variety of synthetic methods have been proposed, the preparation of the nanocomposite film with controlled morphology in a single process has been rarely attempted. Here, we introduce a facile and rapid synthetic method to fabricate the Ag-ZnO nanocomposite films with controlled morphology by using microreactor-assisted solution deposition (MASD) process. The nanocomposite film could be formed in a single process within 10 min, which is enabled by rationally designing the MASD process. In addition, by simply tuning in-situ growth kinetics of ZnO nanostructures in the process, the morphology of the Ag-ZnO nanocomposite film is varied, including flower- and nanorod-structure. The enhanced photocatalytic activity of the Ag-ZnO nanocomposite film over the pristine ZnO counterpart is demonstrated by performing the photoelectrochemical (PEC) measurements.

Introduction

Photocatalytic reactions with optical semiconductors have been extensively studied for several applications such as the photocatalytic water splitting and photocatalytic degradation of organic contaminants.^{1, 2} A variety of metal oxide semiconductors including TiO₂, ZnO, ZrO₂, and perovskite-type metal oxides (SrTiO₃) have been considered promising photocatalysts owing to their high photocatalytic activity, high stability, and non-toxicity.³⁻⁵ Among these metal oxides, TiO₂ is a chemically stable and highly efficient photocatalyst, finding many photocatalytic related applications.⁶⁻⁸ Besides the TiO₂ photocatalyst, ZnO with a similar bandgap to TiO₂ has also been employed as a photocatalyst under UV light irradiation.^{9, 10} However, ZnO is only active under ultraviolet owing to its wide bandgap. The rapid recombination of photo-generated electrons and holes at the ZnO surface also yields a low quantum efficiency, leading to the low photocatalytic efficiency.¹¹ The incorporation of guest materials into the pristine ZnO could be a promising strategy to enhance the photocatalytic efficiency.^{12, 13} In particular, the growth of Ag NPs on the ZnO surface is known to alleviate the recombination of the photo-generated electrons and holes by forming the Schottky barrier at the Ag-ZnO interface.^{14, 15} In addition, the plasmonic absorption of Ag NPs at visible wavelengths could eliminate the wide bandgap issue of the pristine ZnO.¹⁶

A chemical solution deposition (CSD) process has been intensively researched and developed to prepare the Ag-ZnO

nanocomposite with high quality in a cost-effective manner.^{15, 17} In a typical CSD process, a Zn precursor and Ag precursor were introduced in a batch reactor to grow ZnO and Ag NPs simultaneously.¹⁸ Thus, the controlled growth kinetics of Ag NPs and ZnO is difficult to achieve in the conventional CSD process. The ability to control the growth kinetics is critical to obtain the optimal photocatalyst since it enables rational nanocomposite designs. A two-step synthetic approach has been used to fabricate the Ag-ZnO nanocomposite. In this approach, the pristine ZnO was first synthesized, followed by the subsequent growth of Ag NPs on the ZnO surface via the photo-reduction treatment.¹⁶ Although the two-step synthetic approach is feasible for the tailored nanocomposite design, it is not facile, requiring two separated processes, the CSD process for the ZnO formation and the photo-reduction treatment for the growth of Ag NPs. Therefore, an advanced synthetic approach should be developed to fabricate the high-quality Ag-ZnO nanocomposite in a facile and cost-effective manner, along with the ability to readily tune the morphology of the nanocomposite film.

Here, we introduce an advanced approach to the efficient preparation of the Ag-ZnO nanocomposite films with a controlled morphology by adopting a microreactor-assisted solution deposition (MASD) for the first time. The MASD process has provided a rapid and scalable manufacturing platform for synthesizing and depositing nanomaterials to create functional nanostructures.^{19, 20} For the preparation of the Ag-ZnO nanocomposite film, a microreactor is implemented for the ZnO synthesis, and another microreactor is independently set for the growth of Ag NPs. Then, these two individual microreactor streams are combined to make the mixture of ZnO and Ag NPs dispersion, followed by the subsequent delivery of the reactive mixtures onto the substrate to rapidly form the Ag-ZnO

^a Department of Chemical Engineering, Yeungnam University, 280, Daehak-ro, Gyeongsan-si, Gyeongsangbuk-do, South Korea, E-mail: soryu@ynu.ac.kr

^b School of Chemical, Biological & Environmental Engineering, Oregon State University, Corvallis, Oregon, 97331, United States

^c Department of Chemical Engineering, Gyeongsang National University, 501, Jinjudaero, Jinju-si, Gyeongsangnam-do, South Korea, E-mail: Ch_Choi@gnu.ac.kr

† Footnotes relating to the title and/or authors should appear here.

Electronic Supplementary Information (ESI) available: [details of any supplementary information available should be included here]. See DOI: 10.1039/x0xx00000x

nanocomposite film. A key feature of the MASD process is the ability to tailor in-situ reaction kinetics of reactants in a microreactor. Thus, the growth kinetics of both ZnO and Ag NPs could be tailored in the individual microreactor, allowing for the controlled morphology of the Ag-ZnO nanocomposite in a single process. To the best of our knowledge, this is the first study to tailor the morphology of the Ag-ZnO nanocomposite film using microreactors and study the morphology impact on the photoelectrochemical (PEC) performance. The Ag-ZnO nanocomposite films exhibit an enhanced photocurrent response, as compared to the pristine ZnO. These results would offer the MASD process as a general platform to afford the facile and rapid fabrication of the photocatalytic metal-metal oxide nanocomposite film with various morphologies.

Experimental

Fabrication of Ag-ZnO nanocomposite films

Figure 1 shows a schematic of the MASD process for the deposition of Ag-ZnO nanocomposite films. The deposition process consists of a microprocessor-controlled dispensing pump (Ismatec), capillary tubing (1.22 mm ID, Upchurch Scientific), and a micro T-mixer (Upchurch Scientific). In the case of ZnO synthesis, zinc acetate (Sigma-Aldrich), ammonium acetate (Sigma-Aldrich), and sodium hydroxide were used without further purification. Stream 1 (0.005 M zinc acetate and 0.025 M ammonium acetate) and Stream 2 (0.2 M NaOH) were dissolved in deionized (DI) water and initially pumped into a T-mixer. The T-mixer yielded uniform mixing of the reactants. The mixture was then passed through a capillary tubing reactor with a length of 1.3 m. that was immersed in a water bath. The water temperature was maintained at 70 °C during the growth of ZnO NPs. A volumetric flow rate of 14.7 mL min⁻¹ and 6.8 mL min⁻¹ was adopted for the fabrication of the nanocomposite film with flower and NR structure, respectively. For the synthesis of Ag NPs, silver nitrate (Sigma-Aldrich), ammonium hydroxide (30 vol%, Sigma-Aldrich), and formaldehyde (36 vol%, Sigma-Aldrich) were used without further purification. Like to the synthesis of ZnO NPs, precursors solutions of 7 mM AgNO₃/0.19 M ammonium hydroxide in stream 3 and 5 mL HCHO/50 mL DI water in stream 4 were initially pumped into a T-mixer and sent to a capillary tubing reactor with a length of 40 cm. The growth of colloidal Ag NPs was proceeded at a volumetric flow rate of 0.4 mL min⁻¹ and room temperature. The ZnO NP dispersion and Ag NP dispersion synthesized independently in each tubing reactor was mixed at a T-mixer and finally delivered onto the substrate to form the Ag-ZnO nanocomposite films. The substrate was placed on a spin-coater set at 2000 rpm. The deposition time for the nanocomposite film formation was 6 min. and 14 min. on Si/SiO₂ (100 nm) and FTO substrate, respectively. The substrates were treated with O₂ plasma prior to the deposition process to clean the substrate and promote its wettability. For the characterization of the Ag-ZnO nanocomposite films, the nanocomposite films were prepared on Si/SiO₂, and for the measurement of the PEC activity, the nanocomposite films were grown on FTO glass. The residence

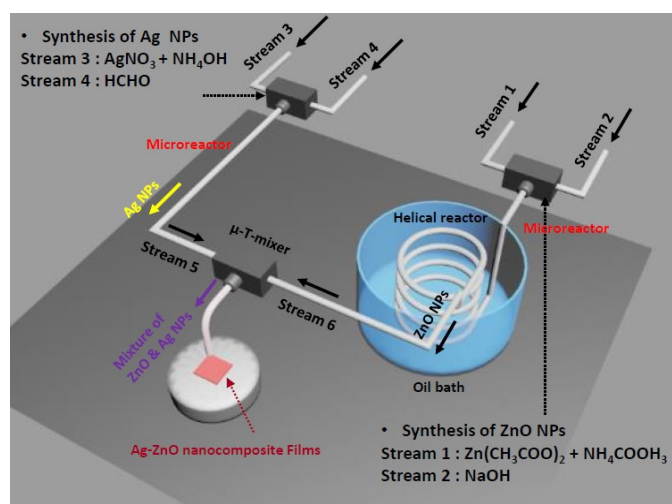


Figure 1. Scheme of the MASD process for manufacturing of the Ag-ZnO nanocomposite films.

time distribution (RTD) of the individual reactant streams in the micro-T mixers is presented in Fig.S1.

Characterizations of the Ag-ZnO nanocomposite

The morphologies of the Ag-ZnO films were examined using scanning electron microscopy (SEM, Quanta 600 FEG). A high resolution transmission electron microscope (HRTEM, FEI TITAN 80-200) equipped with an electron dispersive spectrometer (EDS) and Fast Fourier transform (FFT) was operated at 300 kV. X-ray diffraction (XRD, Bruker D8 discover) was used to study the crystallinity of the films. X-ray photoelectron spectroscopy (XPS, ESCALAB 200-IXL instrument with Mg K radiation) was employed to investigate the elemental composition of the films. The optical properties of the films were studied using a UV-Vis-NIR spectrophotometer (Jasco, V-670). The photoluminescence spectroscopy was performed at room temperature by using 325 nm line of Xe lamp as excitation source (Horiba, iHR550). For the measurement of the optical properties, the films were deposited on a bare soda-lime glass substrate. The thickness of the nanocomposite films was measured by using an alpha-step stylus profiler (Kosaka Laboratory Ltd. ET-3000).

Measurement of PEC performance

The PEC performances were measured using a photocurrent response with on/off light irradiation. The PEC measurements were performed in a three-electrode cell with a flat quartz window to facilitate illumination of the photoelectrode surface. The ZnO or Ag-ZnO films on FTO glass (active area: 1cm²) were used as the working electrodes. A Platinum wire and Ag/AgCl electrode (with saturated KCl) were used as a counter and a reference electrode, respectively. A 0.5M Na₂SO₄ aqueous solution was used as the electrolyte. The PEC responses were measured using a Xe lamp (Light source, ABET technologies LS-150, 150W). The light intensity of 100 mW/cm² is calibrated by a power meter (Powermeter, Newport 1918-R). The current-voltage performances under the chopped light On/Off illumination were measured with a scan rate of 10mV/s during the potential sweep. Photocurrent curves with respect to time were also measured under light on/off illumination at a constant potential of 0.3V.

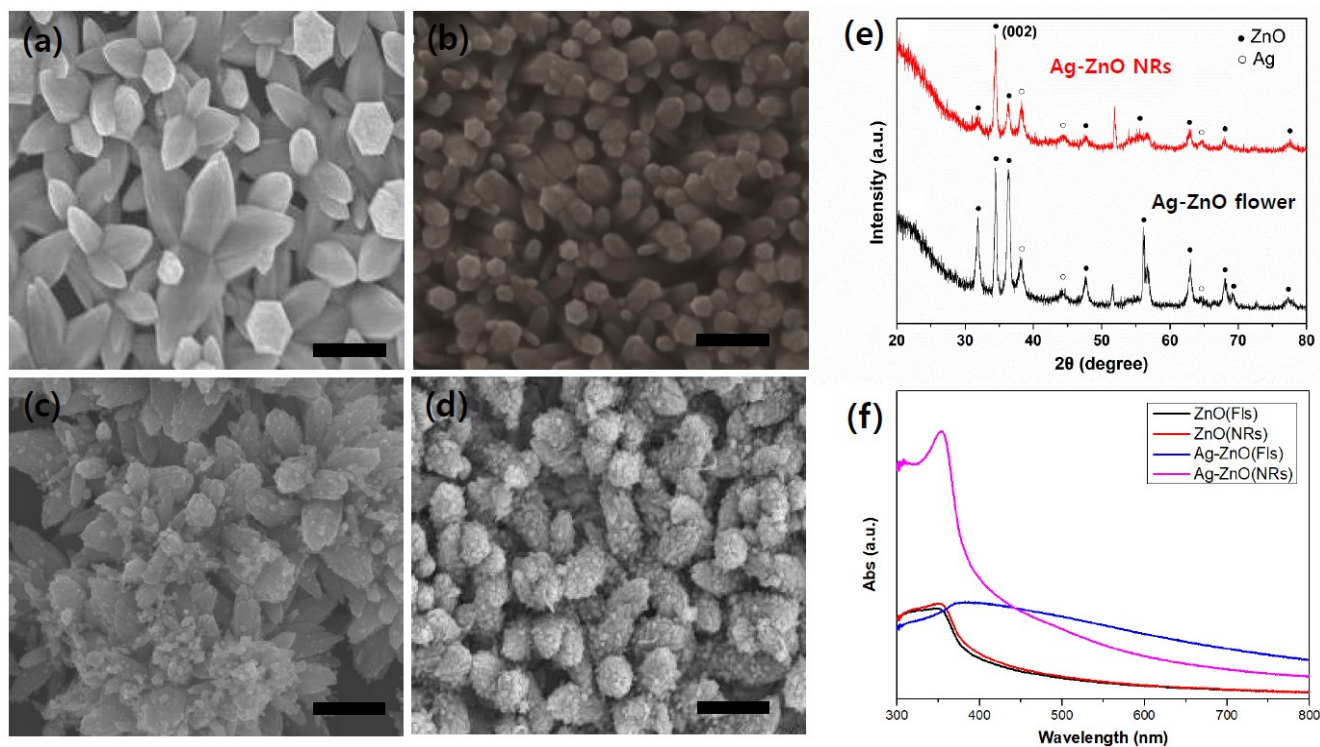


Figure 2. Characteristic results of the Ag-ZnO nanocomposite films: SEM image of (a) pristine flower ZnO, (b) pristine NR ZnO array, (c) flower-like nanocomposite film, (d) NR nanocomposite film, (e) XRD spectra of the nanocomposite films (*:silicon peak), and (f) optical properties of the pristine ZnO films and the nanocomposite films. (scale bar: 500 nm)

Results and discussion

Figure 1 shows the schematic diagram of the MASD process for the fabrication of the Ag-ZnO nanocomposite film. In a previous study, we demonstrated the controlled morphology of ZnO NPs in a continuous flow microreactor by tailoring their growth kinetics, and these ZnO NPs were directly utilized to form ZnO films with various morphologies.²¹ In another study, colloidal Ag NPs were also synthesized in a similar microreactor system and served as a silver ink for the patterning of a highly conductive silver feature.²² By in-situ tuning the growth kinetics of Ag NPs, the stable Ag NPs were formed without using any surfactant at room temperature and then immediately supplied for the Ag film formation. From our previous studies, the flow rate of solution was found to be a key parameter in governing the growth kinetics, morphology, and stability of the nanoparticles. An amorphous ZnO film, flower-like ZnO film, and ZnO NR arrays were formed at a flow rate of 28.1 mL min⁻¹, 14.7 mL min⁻¹, and 6.8 mL min⁻¹, respectively.²¹ For the synthesis of Ag NPs, a flow rate of 0.4 mL min⁻¹ was determined as an optimal flow rate. At a flow rate exceeding 0.4 mL min⁻¹, the primary Ag NPs could not be formed due to extremely short residence time, and a flow rate lower than 0.4 mL min⁻¹ led to the aggregation of colloidal Ag NPs, causing the clogging of a microreactor.²² Based on the previous studies, it is reasonable that directly integrating a microreactor for ZnO synthesis with another microreactor for growing colloidal Ag NPs would give rise to the synthesis of Ag-ZnO nanocomposite NPs, and these nanocomposite NPs could serve as building blocks to form the Ag-ZnO nanocomposite

films. Also, by appropriately adjusting the flow rate of the microreactor responsible for the ZnO synthesis, the morphology of the Ag-ZnO nanocomposite film could be controlled. The flower-like Ag-ZnO nanocomposite film was prepared at a flow rate of 14.7 mL min⁻¹ while the NR Ag-ZnO nanocomposite film was fabricated at a flow rate of 6.8 mL min⁻¹. The flow rate effect on the film morphology is attributed to the fact that the flow rate determines the structure of building blocks that constitute the ZnO films.²¹ Therefore, the microreactor in charge of forming ZnO NPs plays two crucial roles; constituting the ZnO matrix (host) and determining the morphology of the Ag-ZnO nanocomposite film. The total process time from the NP synthesis to the film fabrication is 6 min., proving that our system enables the rapid production of the nanocomposite film in a cost-effective manner. Besides, both ZnO NPs and colloidal Ag NPs are simultaneously synthesized at the individual microreactor in a single process, and thus no additional apparatus is required for the nanocomposite manufacturing. Lastly, the Ag-ZnO nanocomposite film with a different morphology could be obtained by simply adjusting the flow rate of the microreactor, providing the convenience to readily engineer the nanocomposite structure.

First of all, the pristine flower and NR ZnO film were prepared to compare their characteristics and PEC performances to those of the Ag-ZnO nanocomposite counterparts. The highly dense flower structure was deposited on the substrate, and the NR arrays were also grown on the substrate with high density (Figure 2a and b). The XRD pattern exhibits the ZnO NR arrays with a [001] preferred orientation while the flower-like structure was formed in random orientation (Fig.S2). All of the peaks in the XRD spectra are consistent with the reported

pristine ZnO film, indicating that the highly pure ZnO films could be prepared by using the microreactor process.²¹ The SEM images of the Ag-ZnO nanocomposite films are displayed in Figure 2c and d. Even after incorporating Ag NPs into the ZnO matrix, the morphology of the ZnO matrix was found to remain similar. The presence of Ag NPs onto the ZnO structure was clearly seen onto the ZnO surface. (Figure 2c). The incorporation of Ag NPs onto the ZnO structure led to an increase of petal density of the flower. Since the majority of colloidal Ag NPs

flower-like film exhibits the thickness of 563 nm, and for the NR nanocomposite film the thickness of 567 nm was measured. Based on our previous study, it is presumed that the nanorod constituting the NR nanocomposite film has approximately 570 nm and 80 nm in length and diameter, respectively.²³ The optical properties of the nanocomposite films were investigated (Figure 2f). The nanocomposite films exhibit the broad absorption at the visible wavelengths between 400 nm to 800 nm owing to the surface plasmon resonance effect of Ag NPs.¹⁶

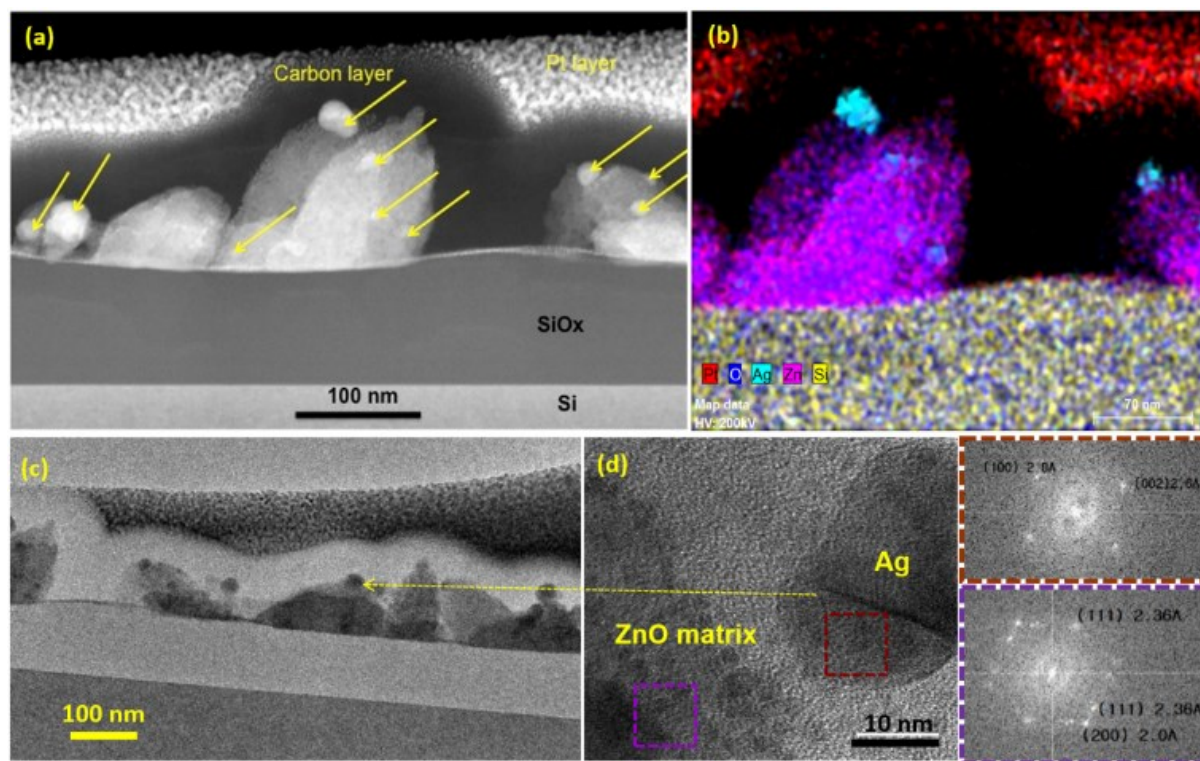


Figure 3. (a) STEM image of a cross-sectional flower-like nanocomposite film (arrows indicate Ag NPs), (b) EDS mapping of the flower-like nanocomposite film, (c) TEM image of a cross-sectional flower-like nanocomposite film, and (d) close view of individual Ag NP onto the ZnO matrix with FFT images.

synthesized at the microreactor system are very small with the size of 2~10 nm in diameter,²² the flower ZnO morphology would not alter significantly. However, Ag NPs may serve as nucleation sites for ZnO growth during the fabrication of the nanocomposite, resulting in the high population of the petals as compared to the pristine ZnO. The incorporation effect on the morphological alteration was also observed for the Ag-ZnO NR nanocomposite film (Figure 2d). One interesting finding is that Ag NPs somewhat disrupt the preferential growth of ZnO NR arrays, as confirmed by the XRD analysis (Figure 2e). While a peak for the (002) plane is exclusively prominent for the pristine ZnO NR array, other peaks at 32° and 36° appear for the Ag-ZnO NR nanocomposite film, which corresponds to (100) and (101) plane of ZnO, respectively. It is speculated that during the formation of the Ag-ZnO nanocomposite, the preferential order of the crystalline ZnO NPs may be impeded by the incorporation of Ag NPs. Although Ag NPs cause a little change on the ZnO matrix morphology, the crystallinity of both ZnO and Ag in the nanocomposite film is high. Very sharp diffraction patterns only attributed to ZnO and Ag are presented, and no other peaks were detected in the XRD spectra. The film thickness of the Ag-ZnO nanocomposite films is provided in Fig.S3. The Ag-ZnO

The bandgap of the pristine ZnO films and the nanocomposite films were estimated by using a Tauc plot method (Fig. S4). The pristine ZnO films exhibit the band gap of 3.2~3.3 eV that agrees well with the reported one.¹¹ For the nanocomposite films, the band gap value depends on the morphology, showing approximately 2.75 eV and 1.90 eV for Ag-ZnO NR and Ag-ZnO flower-like structure, respectively. A typical flower-like Ag-ZnO nanocomposite film was analyzed by using STEM and EDS after a focused ion beam (FIB) lithography (Figure 3). The cross-sectional view of the nanocomposite film displays the petals of the flower and Ag NPs depositing onto the surface of the petals. In addition to Ag NPs onto the petal surface, Ag NPs were also embedded inside the petals of the flower (Figure 3a). The size of individual Ag NPs approximately ranges from 5 nm to 10 nm, and some aggregated Ag NPs were also presented. The corresponding EDS mapping image of the flower petals confirms the synthesis of ZnO and Ag NPs and the incorporation of Ag NPs onto the ZnO surface and inside the ZnO matrix (Figure 3b). The inclusion of Ag NPs into the ZnO matrix was further evidenced by the TEM image (Figure 3c). Consistent with the analysis of the STEM image, Ag NPs are randomly distributed onto and inside the ZnO matrix. An individual Ag NP attached to

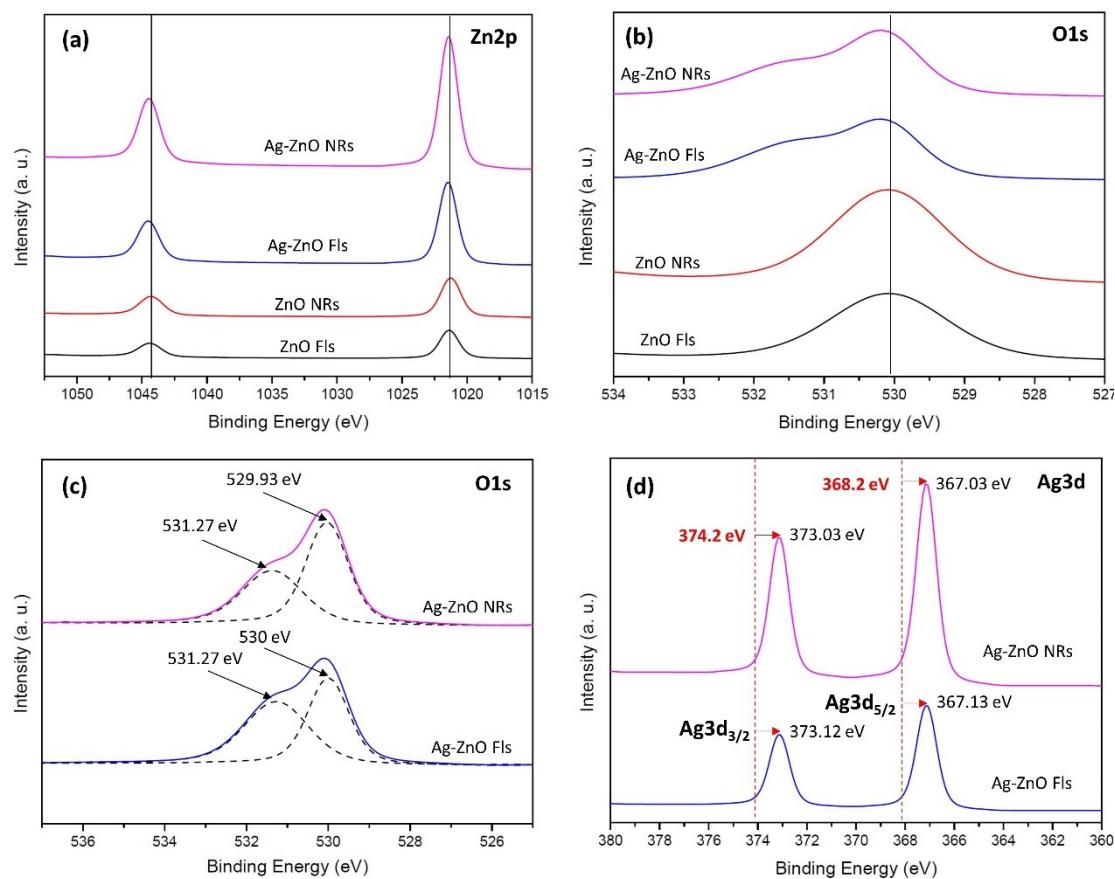


Figure 4. XPS analysis of the nanocomposite films: (a) Zn2p spectra, (b) O1s spectra, (c) fit spectra of O1s, and (d) Ag3d spectra.

the ZnO surface was thoroughly examined by HRTEM (Figure 3d). It was found that the ZnO matrix is composed of polycrystalline ZnO NPs with a d-spacing of 2.36 Å (111) and 2.0 Å (200) whereas the Ag NP shows the single crystalline nature with a d-spacing of 2.0 Å (100) and 1.6 Å (002).²⁴⁻²⁶ We performed XPS analysis to study the chemical composition of the Ag-ZnO nanocomposite film (Figure 4). As compared to the pristine ZnO films, Zn and O binding energy shift to higher binding energy for the Ag-ZnO nanocomposite films. The O1s profile in the Ag-ZnO nanocomposite films is asymmetric and could be deconvoluted, as shown in Figure 4c, which indicates the existence of two different O species in the nanocomposite films. The peak at approximately 531.3 eV is attributed to the lattice oxygen of ZnO, and another peak at a higher binding energy of 532.3 eV is associated with the oxygen of the surface hydroxyls.²⁷ No peak appeared at 529.0 eV, which corresponds to O in Ag₂O.²⁸ This result confirms that the Ag NPs incorporated into the ZnO matrix are pure metallic. A remarkable shift of Ag3d_{5/2} and Ag3d_{3/2} component to lower binding energy was also observed for the nanocomposite films, as compared to pristine Ag NPs (Figure 4d) (The binding energy of Ag3d_{5/2} and Ag3d_{3/2} for the pristine Ag are around 368.2 eV and 374.2 eV, respectively).²⁹ The shift of O1s and Ag3d component to higher and lower binding energy is associated with the strong interaction between Ag NPs and the ZnO matrix. It is known that at the Ag-ZnO interface, electrons transfer from Ag to the conduction band (CB) of ZnO due to the smaller work function of Ag than ZnO.¹⁵ Thus, a new Fermi energy level is formed,

resulting in the higher valence of Ag. All of these characteristic results strongly support the ability of the MASD process to rapidly produce high-quality Ag-ZnO nanocomposite films with controlled morphologies in a facile manner.

Photocatalytic activity of the Ag-ZnO nanocomposite films was evaluated by employing the nanocomposite films as photoanodes in PEC experiment. Figure 5a shows linear sweep voltammograms (LSVs) of the pristine flower ZnO and Ag-ZnO nanocomposite photoanode under dark and light conditions between potential windows of -0.2 to 0.5 V at a scan rate of 10 mV/s in a 0.5M Na₂SO₄ electrolyte. The photocurrent of the illuminated ZnO film is determined by the efficiency of transferring excited electrons from the ZnO film to the FTO layer over their recombination rate at the film surface or electrolyte/film interface. Under illumination, the apparent increment in the photocurrent density relative to the dark state was observed for all the tested photoanodes, indicating that the ZnO films showed the solar light collection to convert it into a photoelectric current. The photocurrent onset potential was at around -0.2 V versus RHE for the pristine and Ag-ZnO nanocomposite films. The photocurrent of the Ag-ZnO nanocomposite films continued to increase with an increase of positive potential and became saturated at around 0.3 V. The photocurrent density of the Ag-ZnO nanocomposite films at 0.2 V is 204.2 μA/cm² and 123.5 μA/cm² for the flower and NR structured nanocomposite film, respectively, which is much enhanced photocurrent density as compared to the pristine flower-like ZnO film with 86.3 μA/cm² at the same potential.

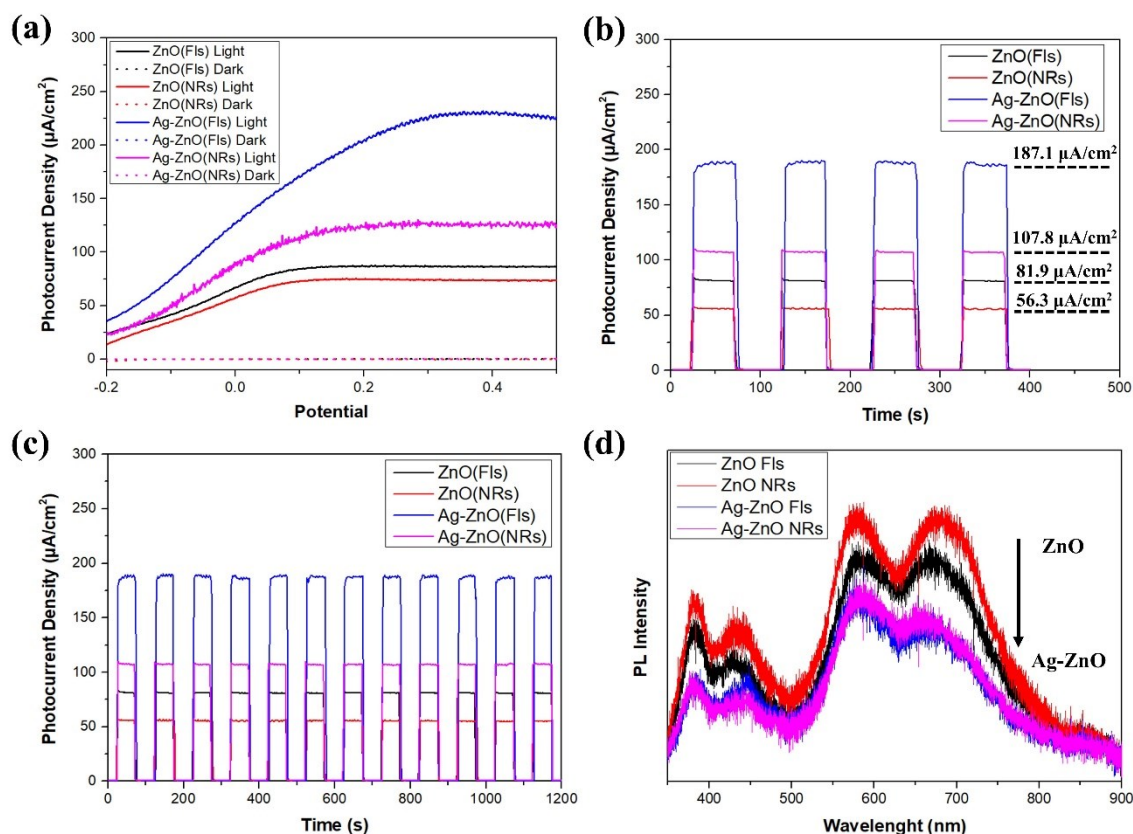


Figure 5. (a) Photocurrent density vs. voltage curves for pristine ZnO, flower nanocomposite film and NR nanocomposite film measured in 0.5M Na_2SO_4 at 100 mW/cm^2 solar simulating light (b) Photocurrent curves with as time measured under light on/off illumination at constant voltage of 0.3V. (c) The photocatalytic stability of the pristine ZnO films and nanocomposite films. (d) PL spectra of pristine ZnO and nanocomposite films at room temperature.

The improved photocurrent of the Ag-ZnO nanocomposite films results from the enhanced separation of photo-induced electron and hole pair, the extended light absorption into visible wavelengths by the surface plasmon resonance (SPR) effect of Ag NPs, and lastly enhanced charge transfer kinetics between Ag and ZnO.¹⁴ The on-off cycle polarization was also performed at a constant voltage of 0.3 V versus RHE (Figure 5b). All of the films exhibited instantly increased photocurrent with the light on, indicating the fast light response and electron transfer under illumination. The flower-like Ag-ZnO nanocomposite film showed the highest values of 187.1 $\mu\text{A}/\text{cm}^2$, followed by 107.8 $\mu\text{A}/\text{cm}^2$ for NR nanocomposite and 81.9 $\mu\text{A}/\text{cm}^2$ for the pristine flower-like ZnO, and 56.3 $\mu\text{A}/\text{cm}^2$ for the pristine ZnO NR film. The flower-like nanocomposite film performed more effectively than the NR nanocomposite counterpart. This is related to the bandgap of the flower-like nanocomposite film. As mentioned before, the bandgap of the flower-like nanocomposite film is lower than that of the NR nanocomposite film, indicating that the flower-like nanocomposite film absorb wider wavelength of visible light as compared to the NR nanocomposite one. Surface area may be also involved in the enhanced PEC performance of the flower-like nanocomposite film. The flower structure may have a larger surface area than the NR structure due to the fact that flower structure grows in a random orientation while the NR one mainly forms in a vertical direction. The PEC activity of the nanocomposite films is compared with reported nanocomposite films prepared by a CSD process. Lin et al.

reported the fabrication of a nanocomposite film with NR structure by combining hydrothermal reaction and photo-reduction treatment.³⁰ The photocurrent density of the nanocomposite film reached to around 380 $\mu\text{A}/\text{cm}^2$ at 0.2V. A conventional hydrothermal reaction was used to fabricate a Ag-implemented ZnO hierarchical nanoflowers that shows the photocurrent density of approximately 95 $\mu\text{A}/\text{cm}^2$ at 0.3V.¹⁸ Kale et al. also fabricated a similar Ag-ZnO hierarchical structure by using a hydrothermal method.¹⁴ The photocurrent density of around 310 $\mu\text{A}/\text{cm}^2$ at 0.3V was obtained from the Ag-ZnO hierarchical structure. The comparison results of the PEC performances confirm that the MASD process enables to fabricate the Ag-ZnO nanocomposite film with comparable PEC activity of 204 $\mu\text{A}/\text{cm}^2$. We believe that the PEC activity could be further improved by optimizing the concentration ratio between ZnO and Ag NP. The aim of this study is to demonstrate the facile and efficient fabrication of the Ag-ZnO nanocomposite film by using the MASD process. It is noteworthy that a conventional hydrothermal process typically requires prolonged reaction time with at least several hours for fabricating Ag-ZnO nanocomposite film whereas the MASD process allows for manufacturing of the nanocomposite film within 10 min.

The photocatalytic stability of the nanocomposite films was investigated by extending the PEC experiment up to 1200 s (Figure 5c). The stability results exhibit that the photocurrent density of all the tested films is consistent without any

noticeable deterioration, indicating that the Ag-ZnO nanocomposite films prepared by the MASD process is photocatalytically stable.

Figure 5(d) compares the room temperature PL spectra between the pristine ZnO films and the Ag-ZnO nanocomposite films. Four emission peaks appeared at 383, 410, 540, and 592 nm. The UV emission at 383 nm could be attributed to the near band edge emission (NBE) of ZnO, and a broad violet emission at 410 nm could be assigned to the electron transition from shallow donor level of neutral zinc interstitial to the top level of the valence band.³¹ The other two emission peaks at the visible region corresponds to bound excitons and defect states located at the surface of ZnO.^{31, 32} As compared to the pristine ZnO films, the emission intensity of the nanocomposite films is decreased, which is consistent with Stern-Volmer quenching.^{31, 33} The quenching of UV emission occurs due to the contact of Ag NP to the ZnO surface where electrons from the conduction band of ZnO transport to Fermi level of Ag NP.¹⁴ The results of the PL spectra indicate a suppression of electron-hole recombination rate by the efficient charge separation, resulting in the enhancement of the PEC activity.³⁴

Conclusions

The Ag-ZnO nanocomposite films with flower and NR structure were fabricated by using microreactor-assisted solution deposition (MASD) process that was rationally designed by using the series of microreactor systems. Two microreactor systems were implemented for separately growing Ag NPs and ZnO NPs, and later the synthesized Ag NP solution and ZnO NP solution were combined at a microreactor to synthesize the Ag-ZnO nanocomposite. The MASD process enabled to fabricate the nanocomposite films with various morphologies in one-pot process within 10 min. The enhanced photocatalytic activity of the Ag-ZnO nanocomposite films over the pristine ZnO film was demonstrated by the PEC experiment.

Acknowledgements

The work at OSU was funded by NSF under grant No. 1707506 and Scalable Nanomanufacturing program under Grant No. CBET-1449383. Part of this work was conducted at OPIC, a National Nanotechnology Coordinated Infrastructure site at the OSU which is supported in part by NSF (grant ECC-1542101) and OSU. The TEM is funded by NSF via MRI Program under Grant No. 1040588. The work in YU is work was supported by the Yeungnam University Research Grant (No.216A380108) in 2016

Notes and references

- G. Wang, H. Wang, Y. Ling, Y. Tang, X. Yang, R. C. Fitzmorris, C. Wang, J. Z. Zhang and Y. Li, *Nano Lett.* 2011, **11**, 3026-3033.
- U. I. Gaya and A. H. Abdullah, *J. Photoch. Photobio. C*, 2008, **9**, 1-12.
- H. Kato and A. Kudo, *J. Phys. Chem. B*, 2002, **106**, 5029-5034.
- D. R. Miller, S. A. Akbar and P. A. Morris, *Sensor. Actuat. B-Chem.* 2014, **204**, 250-272.
- J. Desilvestro and O. Haas, *J. Electrochem. Soc.* 1990, **137**, 5C-22C.
- K. Nakata and A. Fujishima, *J. Photoch. Photobio. C* 2012, **13**, 169-189.
- W. Wang, S. Wang, J. Lv, M. Zhao, M. Zhang, G. He, C. Fang, L. Li and Z. Sun, *J. Am. Ceram. Soc.* 2018, **101**, 5469-5476.
- J. Lv, R. Miao, M. Zhang, G. He, M. Zhao, B. Yu, W. Wang, B. Li and Z. Sun, *J. Mater. Sci.: Mater. Electron.* 2018, **29**, 16282-16288.
- Q. Deng, X. Duan, D. H. Ng, H. Tang, Y. Yang, M. Kong, Z. Wu, W. Cai and G. Wang, *ACS Appl. Mater. Inter.* 2012, **4**, 6030-6037.
- J. Lv, P. Yan, M. Zhao, Y. Sun, F. Shang, G. He, M. Zhang and Z. Sun, *J. Alloy Compd.* 2015, **648**, 676-680.
- V. Srikant and D. R. Clarke, *J. Appl. Phys.* 1998, **83**, 5447-5451.
- J. Lv, W. Wang, M. Zhao, W. Zhu, Y. Cheng, G. He, M. Zhang, X. Chen and Z. Sun, *J. Mater. Sci.: Mater. Electron.* 2017, **28**, 4051-4057.
- J. Lv, J. Xu, M. Zhao, P. Yan, S. Mao, F. Shang, G. He, M. Zhang and Z. Sun, *Ceram. Int.* 2015, **41**, 13983-13987.
- S. S. Patil, M. G. Mali, M. S. Tamboli, D. R. Patil, M. V. Kulkarni, H. Yoon, H. Kim, S. S. Al-Deyab, S. S. Yoon and S. S. Kolekar, *Catal. Today*, 2016, **260**, 126-134.
- C. Ren, B. Yang, M. Wu, J. Xu, Z. Fu, T. Guo, Y. Zhao and C. Zhu, *J. Hazard. Mater.* 2010, **182**, 123-129.
- Z. Han, L. Ren, Z. Cui, C. Chen, H. Pan and J. Chen, *Appl. Catal. B- Environ.* 2012, **126**, 298-305.
- N. Bahlawane, K. Kohse-Höinghaus, T. Weimann, P. Hinze, S. Röhe and M. Bäumer, *Angew. Chem. Int. Ed.* 2011, **50**, 9957-9960.
- B. J. Rani, A. Anusiya, M. Praveenkumar, S. Ravichandran, R. K. Guduru, G. Ravi and R. Yuvakkumar, *J. Mater. Sci.: Mater. Electron.* 2019, **30**, 731-745.
- C. H. Choi, Y. W. Su and C. H. Chang, *CrystEngComm*, 2013, **15**, 3326-3333.
- C.-H. Choi, E. Allan-Cole and C.-h. Chang, *CrystEngComm*, 2017, **19**, 1265-1272.
- C. H. Choi and C. H. Chang, *Cryst. Growth Des.* 2014, **14**, 4759-4767.
- C. H. Choi, E. Allan-Cole and C. H. Chang, *J. Mater. Chem. C*, 2015, **3**, 7262-7266.
- C.-H. Choi, J. B. Levin and C.-h. Chang, *CrystEngComm*, 2016, **18**, 8645-8652.
- B. Mehta, M. Chhajlani and B. Shrivastava, *J. Phys. Conf. Ser.* 2017, **836**, 012050.
- S. Agnihotri, G. Bajaj, S. Mukherji and S. Mukherji, *Nanoscale*, 2015, **7**, 7415-7429.
- V. Dhand, L. Soumya, S. Bharadwaj, S. Chakra, D. Bhatt and B. Sreedhar, *Mat. Sci. Eng. C*, 2016, **58**, 36-43.
- W. Lu, S. Gao and J. Wang, *J. Phys. Chem C*, 2008, **112**, 16792-16800.
- J. F. Weaver and G. B. Hoflund, *Chem. Mater.* 1994, **6**, 1693-1699.
- S. Kandula and P. Jeevanandam, *RSC Adv.* 2015, **5**, 76150-76159.
- Z. Mu, W. Yan, R. Zhao and Y. Lin, *Mater. Res. Express*, 2015, **2**, 065008.

ARTICLE

Journal Name

31. A. Amutha, S. Amirthapandian, B. Sundaravel, B. Panigrahi, K. Saravanan and P. Thangadurai, *J. Appl. Phys.* 2016, **120**, 205104.
32. W. I. Park and G. C. Yi, *Adv. Mater.* 2004, **16**, 87-90.
33. F. X. Redl, K.-S. Cho, C. B. Murray and S. O'Brien, *Nature*, 2003, **423**, 968.
34. J. Lv, Q. Zhu, Z. Zeng, M. Zhang, J. Yang, M. Zhao, W. Wang, Y. Cheng, G. He and Z. Sun, *J. Phys. Chem Solids*, 2017, **111**, 104-109.